International Journal of Multiphase Flow 100 (2018) 155–171

Contents lists available at ScienceDirect

International Journal of Multiphase Flow

journal homepage: www.elsevier.com/locate/ijmulflow

A physical study of air–water flow in planar plunging water jet with large inflow distance

Numa Bertola[a,b], Hang Wang[a,*], Hubert Chanson[a]

[a] The University of Queensland, School of Civil Engineering, Brisbane QLD 4072, Australia
[b] ETH-Zürich, Future Cities Laboratory, Singapore

ARTICLE INFO

Article history:
Received 23 June 2017
Revised 13 September 2017
Accepted 21 December 2017
Available online 22 December 2017

Keywords:
Plunging water jet
Air entrainment
Impact velocity
Pre-aeration
Phase-detection probe

ABSTRACT

A plunging jet is commonly encountered in nature. It is also widely used in industry for its capacity to enhance fluid mixing and entrain gases into the liquid fluid when the impact velocity exceeds a critical value. This paper presents a physical study of vertical supported planar water plunging jets, in a relatively large-size facility. Air-water flow properties were measured in the falling jet and in the plunging pool using an intrusive phase-detection probe, with jet impact velocities between 2.5 m/s and 7.4 m/s and a fixed jet length. The falling jet was characterised by large disturbance and substantial pre-aeration. Intense air-water mixing was observed downstream of the impingement point. The development of air diffusion layer and turbulent shear layer was characterised by the streamwise evolution of void fraction, bubble count rate, bubble chord length and interfacial velocity profiles. The results compared favourably with the literature, albeit some difference was observed associated with different inflow jet turbulence levels as well as instrumentation development and signal processing refinement, including instrumental size, scanning rate and duration. The clustering properties were derived using the near-wake criterion. Results were comparable to those in horizontal hydraulic jumps. The air-entrainment rate was derived, highlighting the significant contribution of jet pre-aeration.

1. Introduction

The impingement of a rapid jet into a slower body of fluid is known as a plunging jet. Examples of plunging jet situations include a vertical plunging jet, a horizontal hydraulic jump, a breaking tidal bore, and a liquid jet impacting a solid or moving boundary. Fig. 1 illustrates a plunging breaking wave (Fig. 1a) in the ocean and a planar jet flowing down a drop structure in an artificial waterway (Fig. 1b). A key feature of plunging jet flow is the associated air entrainment taking place at the plunge point when the impact velocity exceeds a critical value (McKeogh and Ervine 1981; Cummings and Chanson 1999). The entrainment of air is affected by a number of factors including the fluid properties, jet velocity and instability, and any form of pre-aeration prior to the jet impingement (Ervine 1998; Kiger and Duncan 2012). The examples in Fig. 1 show some highly-aerated jets due to free-surface breaking and large-scale turbulence, which are typically seen in nature and large-size man-made structures.

It is common that a real-life plunging jet application is characterised by relatively large jet disturbance and substantial pre-aeration, such as in hydraulic structures (e.g. dam spillways), wastewater treatment plants, fish farming industries, etc. In these cases, highly turbulent jet conditions are favourably adopted to facilitate air-water exchange thus water re-oxygenation. In other occasions, the entrapment of air particles by the liquid jet is disadvantageous thus the inflow jet conditions require careful control, like in food industry, steel industry and the nuclear reactor containment cooling systems (Kirchner 1974; Van De Donk 1981). With the occurrence of major air entrainment events, the entrained air bubbles are advected in large-scale vortical structures into deep water before being dispersed or driven to free-surface by buoyancy (Bin 1993; Chanson 1997). The bubble breakup, coalescence and recirculation play critical roles in the enhancements of mass and heat transfer and energy dissipation (Kirkpatrick and Lockett 1974). The bubble-turbulence interplays are complicated physical processes of which a comprehensive description requires a great number of parameters to be considered, while our current knowledge is still far from a full understanding (Van de Sande and Smith 1976; Ervine 1998; Kiger and Duncan 2012; Wang et al., 2017).

The bubble entrainment mechanisms have been studied experimentally for a range of jet conditions (e.g. fluid viscosities and salinity, jet speeds, jet disturbance levels), albeit most studies

---

[*] Corresponding author.
E-mail address: hang.wang@uqconnect.edu.au (H. Wang).

https://doi.org/10.1016/j.ijmultiphaseflow.2017.12.015
0301-9322/

Fig. 1. Photographs of plunging jet applications and air entrainment: (A, left) Plunging breaking wave at Main Beach, North Stradbroke Island (Australia); (B, right) Drop structures at Jiufen Township (Taiwan, China).

focused on circular jets (Van de Sande and Smith 1973; Zhu et al., 2000; Chirichella et al., 2002; Soh et al., 2005; Chanson et al., 2006). Physical studies of the bubbly flow region beneath the receiving water surface encompassed flow imaging, laser Doppler velocimetry, particle imaging velocimetry and phase-detection probes (McKeogh and Ervine 1981; Bonetto and Lahey 1993; Cummings and Chanson 1997a,b; Brattberg and Chanson 1998, Qu et al. 2011). The experimental data enabled a better understanding of air entrainment mechanisms and bubble transport regimes, and provided validation data sets for computational multiphase flow models (Richards et al., 1994; Ervine 1998; Bombardelli 2012). Despite the variety of plunging jet configurations, an overall conclusion was that large amount of air bubbles were entrained, with the majority of bubbles in the aerated flow region having radii in the order of a millimetre. The bubble-turbulence interplay, however, has not been investigated in fine details at large physical scales, because of the complexity of air-water flow motion as well as the limitation of two-phase flow measurement techniques.

The present work was motivated by the major advances in experimental methodology and data processing techniques in the past two decades. Supported planar (quasi-two-dimensional) water jets were investigated physically. The air-water flow properties were measured with an intrusive phase-detection probe in the highly-aerated turbulent shear region underneath the impingement point for several impact velocities of 2.5 m/s, 3.8 m/s, 5.6 m/s and 7.4 m/s. The planar jet configurations were comparable to those used by Cummings and Chanson (1997a,b) and Brattberg and Chanson (1998), while the new instrumentation allowed for a significant increase in sampling duration from 3 s to 90 s and further derivation of higher-level turbulence properties (e.g. bubble size spectra, bubble clustering properties, turbulence intensity and characteristic time scales) that provided a better characterisation of the bubble-turbulence interaction. The relatively large-size receiving tank minimised boundary constraint to the flow development. The present jet conditions were characterised by relatively large surface roughness, high jet pre-aeration and some three-dimensional disturbance structures, evidenced by detailed falling jet measurements with different instruments. Such jet conditions are representative in a huge number of hydraulic and water engineering applications, yet not many physical data are available in fundamental investigations.

2. Experimental facility and instrumentation

2.1. Dimensional consideration

The relevant dimensional parameters involved in the physical modelling of vertical two-dimensional plunging jets encompass the fluid properties, boundary conditions, inflow conditions, local two-phase flow properties including microscopic turbulent flow properties, macroscopic free-surface and time dependant flow properties, and physical constants. A simple dimensional analysis may yield a series of dimensionless relationships in terms of the air-water flow properties at a location (x, y) beneath the plunge point:

$$C, \frac{Fd_1}{V_1}, \frac{V}{V_1}, \frac{v'}{V_1}, \frac{T_{xx}V_1}{d_1}, \frac{F_{clu}d_1}{V_1}, \frac{q_{air}}{V_1 d_1}, \ldots$$
$$= F\left(\frac{x-x_1}{d_1}, \frac{y}{d_1}, \frac{x_1}{d_1}, \frac{{v_1}'}{V_1}, \frac{V_1}{\sqrt{gd_1}}, \frac{\rho_w V_1 d_1}{\mu_w}, \frac{g{\mu_w}^4}{\rho_w \sigma^3}, \ldots\right) \quad (1)$$

where C is the void fraction, F is the bubble count rate, d_1 is the jet thickness at impingement, V_1 is the jet impact velocity, V is the time-averaged interfacial velocity, v' is a characteristic turbulent velocity, T_{xx} is an auto-correlation time scale, F_{clu} is the one-dimensional bubble cluster count rate, q_{air} is the air flux, x is the longitudinal coordinate, y is the normal coordinate, x_1 is the free-jet length, ${v_1}'$ is a characteristic jet turbulent velocity at impingement, g is the gravity constant, ρ_w is the water density, μ_w is the water dynamic viscosity and σ is the surface tension between air and water, with the subscript 1 referring to the impingement location.

In Eq. (1), right-hand side, the fifth, sixth and seventh dimensionless terms are the Froude number Fr, Reynolds number *Re* and Morton number Mo, respectively. Note indeed that the Weber number We was replaced by the Morton number based on the Π-Buckingham theorem since $Mo = We^3 Fr^{-1} Re^{-4}$ (Kobus 1984). When the same fluids are used in laboratory and prototype, the Morton number becomes an invariant. Traditionally, plunging jets are studied based on a Froude similarity (Henderson 1966). However, air-water turbulent shear flows are dominated by viscous effects and mechanisms of breakup and coalescence are dominated by surface tension forces. Thus a true air-water flow dynamic similarity requires identical Froude, Reynolds and Morton numbers in both laboratory and prototype: that is impossible unless working at full scale (Chanson 2013). Herein detailed air-water flow experiments were conducted in a relatively large-size facility operating with $3 \times 10^4 < Re < 1 \times 10^5$, ensuring that the results may be extrapolated with negligible scale effects (Rao and Kobus 1971; Wood 1991; Chanson 1997, 2013).

2.2. Experimental facility setup

A new series of experiments were conducted to investigate the air entrainment and turbulence in a vertical supported plunging jet (Fig. 2). The experimental apparatus consisted of a planar water jet issued from a 0.269 m by 0.012 m rectangular nozzle, discharg-

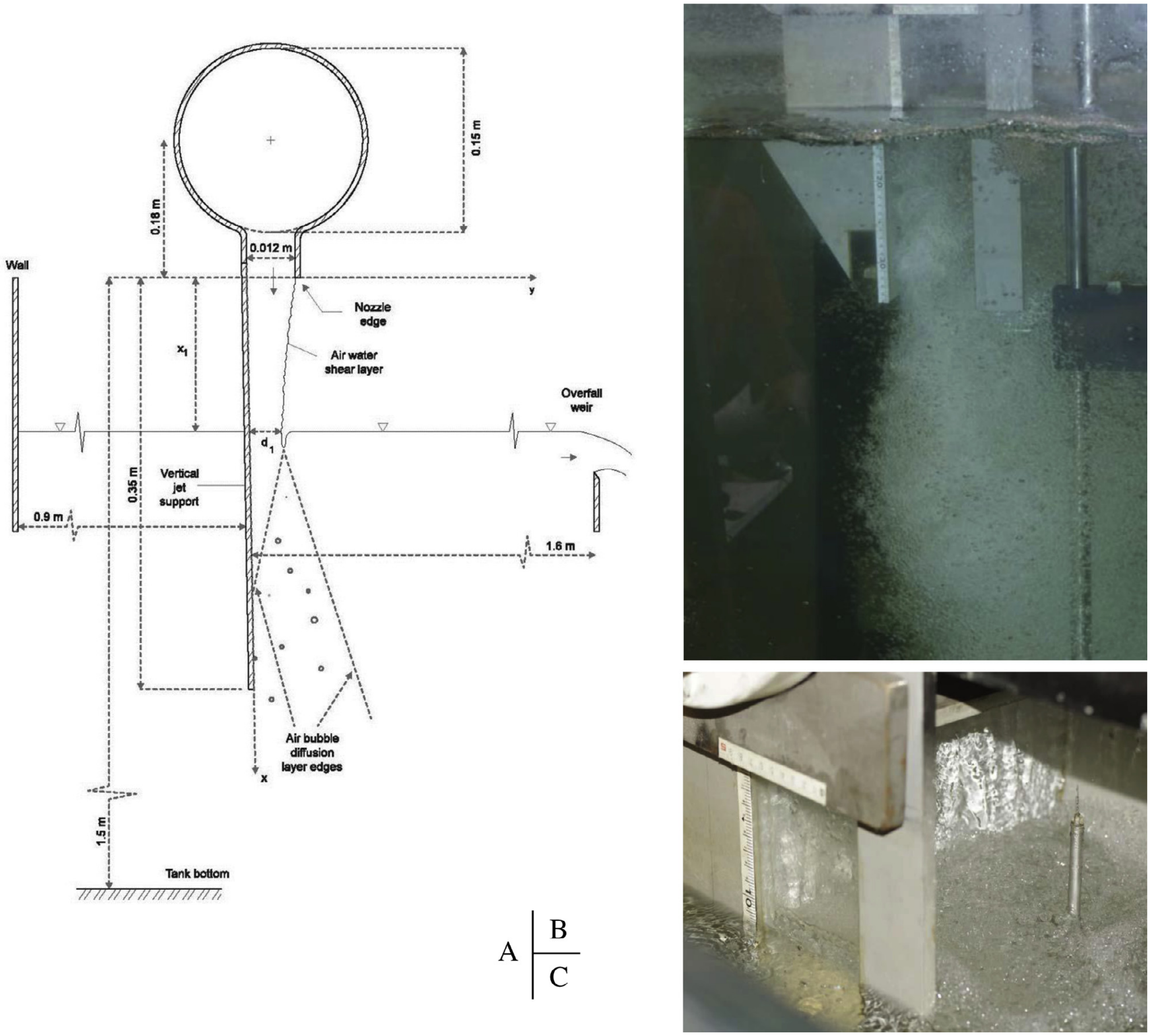

Fig. 2. Experimental facility: (A, left) Side view sketch of the supported plunging jet facility; (B, top right) Air entrainment in plunging pool for impact velocity $V_1 = 3.8$ m/s and jet length $x_1 = 0.1$ m; (C, bottom right) Dual-tip phase-detection probe and plunging jet with impact velocity $V_1 = 2.5$ m/s and jet length $x_1 = 0.1$ m.

ing downwards into a 2.5 m long, 1 m wide, 1.5 m deep receiving tank. The planar jet was supported by a 0.35 m long, full-width PVC sheet extending from the nozzle edge with lateral perspex windows. The jet support had an angle of 88.5° with the horizontal to prevent flow detachment from the support. The plunging jet experimental apparatus is presented in Fig. 2. The same nozzle was previously used by Cummings and Chanson (1997a,b) and Brattberg and Chanson (1998) in a narrower receiving pool.

Water was supplied from two different sources: either a constant head tank delivering water discharges up to 0.0137 m^3/s, or a high-head pump providing flow rates up to 0.038 m^3/s. The water discharge was measured with orifice/Venturi meters installed in the supply pipelines and calibrated on-site. The flow rate readings were further checked against the integration of velocity distributions on the jet centreline. A difference between 2% and 7.5% was shown depending on the flow rate, which is likely linked to the non-uniform jet thickness distribution in the transverse (spanwise) direction.

Two fine adjustment travelling mechanisms were used to control the displacement of any flow-measuring probes in the directions along the jet and normal to the jet support. The probe position was read from two Lucas Schaevitz Magnarule Plus^{TM} sensors with accuracy within 0.05 mm.

2.3. Instrumentation and data processing

The free-falling jet conditions were characterised in terms of jet thickness and surface fluctuations, time-averaged velocity profiles, an estimate of velocity fluctuations, pre-air entrainment, and total pressure distributions. The jet thickness was measured using Microsonic^{TM} Mic+25/IU/TC acoustic displacement meters (ADMs). The non-intrusive ADM sensors had a measurement range of 30 to 250 mm from the detected surface and an accuracy of 0.18 mm. The sensors were sampled at 50 Hz for 180 s at each measurement location. Erroneous sample points caused by non-vertical water surface or splashing droplets were removed manually using a cut-off set at five times the standard deviation about the mean. Clear-water velocity data were collected using a Prandtl-Pitot tube (Dwyer® 166 Series) with a 3.2 mm diameter tube featuring a hemispherical total pressure tapping (Ø = 1.2 mm) and four equally spaced static pressure tappings (Ø = 0.5 mm). The air-water flow velocity data were recorded using a dual-tip phase-detection probe that will be described in detail later. Both velocities, measured by Prandtl-Pitot tube in clear water and phase-detection probe in air-water flow, were compared with the velocity measured independently by a miniature total pressure sensor, as well as the value deriving from flow rate measurement, showing good agreement between different instruments. The comparison also confirmed equal velocities for water and air-water interfaces, in the high-speed two-phase flow regions. The total pressure sensor, manufactured on a micro-electro-mechanical system (model MRV21, MeasureX), had a 5 mm outer diameter, with a 1 mm diameter silicon diaphragm on the sensor tip. The pressure sensor provided an absolute pressure measurement range between 0 and 1.5 bars and a 0.5% precision. It was sampled at 2 kHz for 180 s. The output voltage was temperature and ambient-pressure sensitive, thus a static calibration was conducted twice per day. Combining the total pressure, void fraction and velocity data, the turbulence level of the water flow was derived following Zhang et al. (2016). All measurements were taken on the jet centreline.

The air-water flow properties in the plunging pool were recorded using a dual-tip phase-detection probe, as used in the free-falling jet (Fig. 2C). The phase-detection probe was equipped with two needle sensors, each sensor consisting of a silver inner electrode (Ø = 0.25 mm) and stainless steel outer electrode (Ø = 0.8 mm). The leading sensor tip was $\Delta x = 6.9$ mm ahead from the trailing sensor tip, and the two sensors were aligned with the streamwise direction. Both sensors were excited simultaneously at 20 kHz per sensor for 90 s. The sampling rate and duration were derived from a sensitivity analysis (Bertola et al., 2017). Measurements were taken at eight cross-sections perpendicular to the jet support, between the impingement point and the end of jet support ($0 < x\text{-}x_1 < 0.35$ m), and at three cross-sections further downstream of the end of jet support ($x\text{-}x_1 > 0.35$ m), all on the channel centreline.

The phase-detection probe sensors discriminated between air and water phases based on the different electrical resistance of air and water. The voltage signal was converted into instantaneous void fraction data using a single threshold technique, the threshold being set at 50% of the air-water range. A number of air-water flow properties were derived from the thresholded signal analysis: i.e., time-averaged void fraction C, bubble count rate F, probability density function of bubble chord length, and bubble clustering properties. Further air-water flow properties were derived from a correlation analysis conducted on the raw voltage signal: i.e., time-averaged air-water interfacial velocity V, turbulence intensity Tu and auto-correlation time scale T_{xx}. The time-averaged air-water interfacial velocity was calculated as

$$V = \frac{\Delta x}{T} \tag{2}$$

where T is the time lag for which the normalised cross-correlation function is maximum, thus it represents the average interfacial travel time between the two probe sensors over a distance Δx. The interfacial turbulence intensity Tu, defined as the ratio of velocity standard deviation v' to local time-averaged velocity V, was derived from the relative shape of the cross-correlation function compared to the auto-correlation function (Chanson and Toombes 2002). After simplification, it yielded:

$$Tu = 0.851\frac{\sqrt{{\tau_{0.5}}^2 - {T_{0.5}}^2}}{T} \tag{3}$$

where $\tau_{0.5}$ is the time lag for which the normalised cross-correlation function is half of its maximum value: $R_{xy}(T + \tau_{0.5}) = R_{xy}(T)/2$, with $R_{xy}(T)$ the maximum cross-correlation coefficient observed for a time lag $\tau = T$, and $T_{0.5}$ is the time lag for which the normalised auto-correlation function equals 0.5. The auto-correlation time scale T_{xx} was derived from the integration of the auto-correlation function R_{xx} up to the first zero-crossing:

$$T_{xx} = \int_0^{\tau(R_{xx}=0)} R_{xx}\,d\tau \tag{4}$$

In the air-water flow, the fluctuations of total pressure data may be related to the time-averaged velocity V, void fraction C and velocity fluctuations v' by:

$$p_t{}' = \frac{1}{2}(1 - C)\rho_w\left(V^2 + v'^2\right) + p_s{}' \tag{5}$$

where $p_t{}'$ and $p_s{}'$ are standard deviations of total pressure and static pressure, respectively. By re-arranging Eq. (5), the water-phase turbulence intensity $Tu_p = v'/V$, the subscript p denoting the total pressure measurement, may be expressed as (Zhang et al., 2016):

$$Tu_p = \sqrt{\frac{\frac{p_t{}'^2}{\rho_w{}^2 V^4} - \frac{(1-C)C}{4}}{(1 - C)\left(1 + \frac{C}{2}\right)}} \tag{6}$$

when higher orders of Tu_p were ignored.

Further details on the experimental facility and instrumentation were reported in Bertola et al. (2017), while Appendix I presents a comparative summary.

2.4. Measurement uncertainties

The accuracy of the experiment was sensitive to the measurement uncertainty of water discharge or jet impact velocity, which was further affected by the fluctuating nature of the flow and its aeration processes. The macroscopic, pseudo-periodic flow motions, such as the oscillations of impingement point position and the formation of large vortices in the shear flow, also influenced the correlation analysis thus the quantification of turbulence intensity and auto-correlation time scale (Wang et al., 2014). The effects differed for different parameters and were dependent of relative measurement locations. The instrumental error on void fraction and bubble count rate measurements was estimated to be less than 2% using the phase-detection probe with adopted sampling rate and duration. The error on interfacial velocity measurements with a dual-tip probe was no greater than 5% in high-speed, constant-direction aerated flow regions with $0.05 \langle C < 0.95$ (Cummings & Chanson 1997b). For $C < 0.05$ or $C \rangle 0.95$, longer sampling duration was required to achieve the same level of accuracy. Compared to the effects of the fluctuating motions of the flow, the accuracy of instrumentation was high and the associated measurement error could be ignored.

2.5. Experimental flow conditions

Four impact velocities $V_1 = 2.5$ m/s, 3.8 m/s, 5.6 m/s and 7.4 m/s were investigated for a constant jet length $x_1 = 0.1$ m. Here V_1 is the cross-sectional averaged velocity at the impingement point. Table 1 summarises the flow conditions. In Table 1, the jet thickness d_1 at $x = x_1$ equals to the equivalent clear-water thickness d_e calculated from velocity and void fraction profiles. It was found to be slightly larger than the theoretical jet thickness given by the Bernoulli equation, likely due to the spanwise non-uniform jet thickness distribution, i.e. a thicker jet on the centreline than next to the jet support sidewalls. The non-uniformity was also related to the formation of unsteady three-dimensional structures in the jet, especially at large flow rates. The interaction of these structures with the jet support boundary led to some large air content and correlation coefficients between air-water signals next to the jet support, which was unique for the present high-disturbance

Table 1
Experimental flow conditions.

Q (m^3/s)	d_0 (m)	V_0 m/s)	x_1 (m)	d_1 (m)	V_1 (m/s)	Fr (-)	*Re* (-)	We (-)
0.0067	0.012	2.07	0.10	0.0104	2.49	7.8	2.6×10^4	9.1×10^2
0.0114	0.012	3.53	0.10	0.0115	3.80	11.3	4.4×10^4	2.3×10^3
0.0174	0.012	5.42	0.10	0.0127	5.55	15.9	7.1×10^4	5.5×10^3
0.0236	0.012	7.27	0.10	0.0127	7.43	21.0	9.4×10^4	9.7×10^3

Notes: Q: flow rate; d_0: jet thickness at nozzle; V_0: jet velocity at nozzle; x_1: jet length; d_1: jet thickness at impingement point; V_1: impact velocity; Fr: Froude number, $Fr = V_1 g^{-0.5} d_1^{-0.5}$; *Re*: Reynolds number, $Re = \rho_w V_1 d_1 \mu_w^{-1}$; We: Weber number, $We = \rho_w V_1^2 d_1 \sigma^{-1}$.

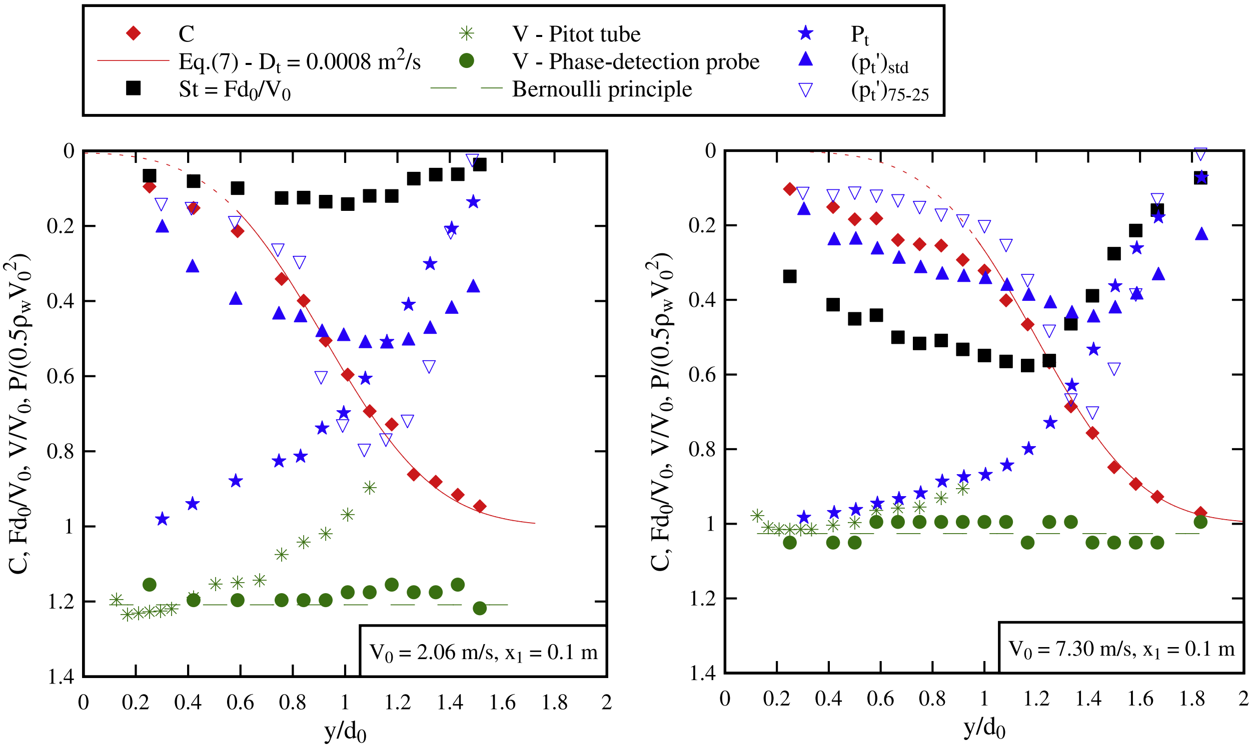

Fig. 3. Characteristics of free-falling jets in terms of air entrainment and velocity distributions measured at x = 0.1 m on jet centreline: (A, left) $V_0 = 2.06$ m/s; (B, right) $V_0 = 7.30$ m/s. (For interpretation of the references to colour in this figure legend, the reader is referred to the web version of this article.)

inflow conditions. A comparison between present and past investigations of planar supported plunging jets is presented in Appendix I.

3. Free-falling jet conditions

The characteristics of the free-falling jet may influence the air entrainment and turbulence development in the plunge pool. The jet flow conditions were thus characterised in detail at several longitudinal positions downstream of the nozzle. Typical measurement results at x = 0.1 m are plotted in Fig. 3 for two nozzle velocities $V_0 = 2.06$ m/s and 7.30 m/s, including void fraction C, bubble count rate F, velocities by Prandtl-Pitot tube and dual-tip phase-detection probe, time-averaged total pressure P_t and its fluctuations. In Fig. 3, y is the distance normal to the jet support and d_0 is the nozzle thickness.

Air entrainment along the jet free-surface was observed for all investigated flow conditions. Air-water flow measurements indicated substantial free-surface aeration starting immediately downstream of the nozzle. The results of time-averaged void fraction C and dimensionless bubble count rate Fd_1/V_1 at x = 0.1 m are shown in Fig. 3. Between the positions Y_{50} and Y_{90} where the void fraction equals 50% and 90% respectively, the void fraction data showed good agreement to the analytical solution of advective diffusion equation for air bubbles in high-speed water jet discharging into air (Chanson 1997):

$$C = \frac{1}{2}\left(1 + \mathrm{erf}\left(\frac{y - Y_{50}}{\sqrt{D_t \frac{x}{V}}}\right)\right) + \frac{1}{2}\left(1 - \mathrm{erf}\left(\frac{y + Y_{50}}{\sqrt{D_t \frac{x}{V}}}\right)\right) \tag{7}$$

where D_t is a bubble diffusivity assumed independent of the horizontal position y, V is the free-stream velocity and erf() is the Gaussian error function. Eq. (7) is compared with the experimental data in Fig. 3. On the other hand, for $y < Y_{50}$ at x = 0.1 m, the observation showed higher void fraction than the theoretical prediction, unlike previous studies (e.g. Brattberg and Chanson 1998). This implied additional air entrainment processes to a pure free-surface aeration, which could be linked with the random formation of three-dimensional disturbance structures along the jet associated with a non-uniform flow field in the nozzle. The presence of these large structures and their movements in the transverse direction might allow temporarily air in between the falling jet and the jet support (as well as lateral support sidewalls), leading to a different pre-aeration pattern. The average turbulence diffusivity D_t deduced from best-fit data was also typically larger than that in a jet flow with simple interfacial aeration. Independent of the nozzle velocity V_0, the present diffusivity data increased along the jet:

$$\frac{D_t}{V_0 d_0} = 0.00318 \frac{x}{d_0} \quad \text{for } 2.5 < \frac{x}{d_0} < 8.3 \tag{8}$$

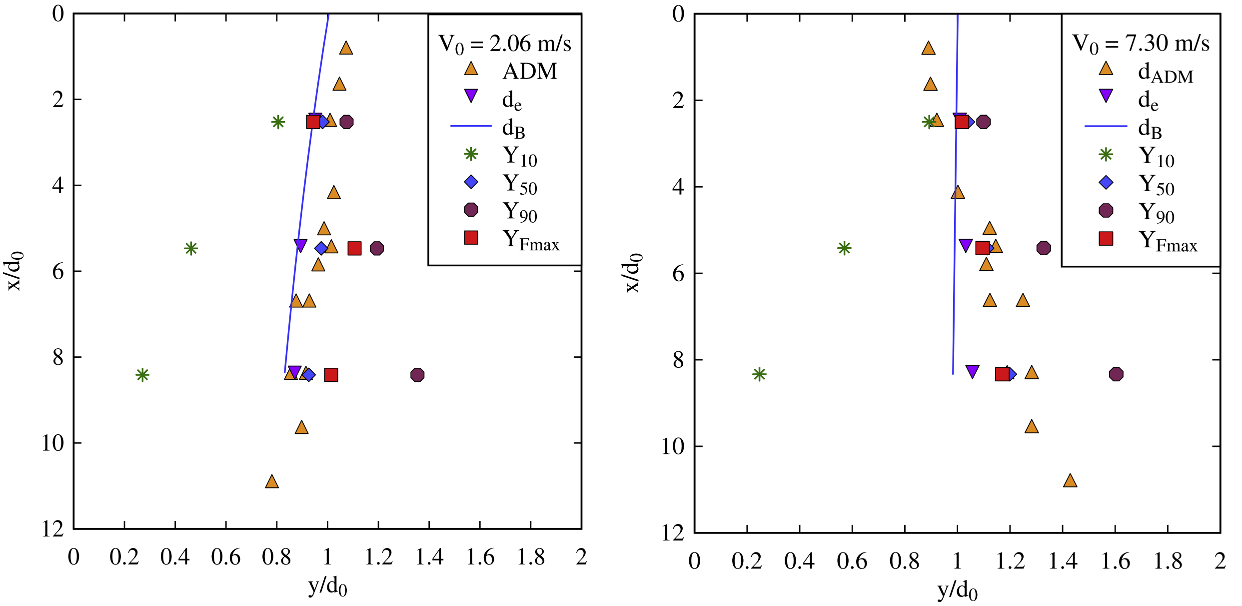

Fig. 4. Dimensionless distribution of supported free-falling jet thickness d/d_0 – Comparison between experimental measurements and theory: (A, left) $V_0 = 2.06$ m/s; (B, right) $V_0 = 7.30$ m/s.

The bubble count rate distributions showed a marked maximum F_{max} at about 50% of time-averaged void fraction ($y = Y_{50}$). The results further showed increasing bubble count rates with increasing nozzle velocity at a given location. As air bubbles diffused through the jet thickness, the bubble count rate distributions tended to become more homogeneous with increasing longitudinal distance.

The bubble chord length is given by the time of a bubble spent on the phase-detection probe sensor tip multiplied by the local interfacial velocity. A statistical analysis of bubble chord length indicated a skewed spectral distribution with a preponderance of small bubble chords relative to the mean size. While a broad range of bubble chord lengths was observed for all impact velocities and all jet locations, the largest probabilities of bubble chord lengths were between 0 and 3 mm. With increasing streamwise distance from the jet nozzle, the proportion of large bubble chord length increased and that of small bubble chord length decreased, independently of the nozzle velocity and local void fraction. Further smaller bubble chords were observed for the larger jet velocities at a given distance from the nozzle.

Velocity measurements showed that the velocity distributions were uniform for all investigated flow conditions, albeit the closest measurement location was $y = 1.6$ mm with the Prandtl-Pitot tube. Boundary friction along the jet support would lead to the development of a turbulent boundary layer, and the present jet flows were partially-developed with thin developing boundary layers: i.e., $\delta/d_0 < 0.2$ for $x/d_0 < 8.3$. In the less aerated flow region, the free-stream velocities measured by the Prandtl-Pitot tube and the phase-detection probe compared favourably with the application of the Bernoulli principle to a vertical jet, while the Prandtl-Pitot tube data were affected adversely by the free-surface air entrainment with increasing distance from the jet support (Fig. 3). Further air entrainment rate in the jet prior to impingement can be calculated based on the void fraction and velocity profiles and the results are presented in Section 5.

The time-averaged total pressure P_t and pressure fluctuations p_t' were recorded at the same locations as phase-detection probe data. The total pressure fluctuations were estimated by two methods: (1) as the standard deviation of the data set, $(p_t')_{std}$, and (2) as the difference between third and first quartiles divided by 1.3, $(p_t')_{75-25}$. For a Gaussian distribution of the pressure data set about the mean, the two values would be equal: i.e. $(p_t')_{75-25} = (p_t')_{std}$. The total pressure was basically constant in the clear-water free-stream flow region (not shown), and it decreased with increasing distance from the jet support in the aerated flow region. Comparison between the total pressure and the kinetic pressure given by local velocity data indicated negligible static pressure in the jet. The total pressure fluctuations were uniformly distributed in the non-aerated free-stream region, but increased in the air-water flow region up to a maximum because of the instantaneous pressure drops caused by the impact of air cavities on the total pressure sensor. The same pattern was observed for both $(p_t')_{std}$ and $(p_t')_{75-25}$.

An estimate of turbulence intensity in the aerated jet using Eq. (6) suggested Tu_p in an order of 10^{-1}, although the accuracy was affected by the difference between the void fraction measured by the phase-detection probe (i.e. C in Eq. (6)) and the actual percentage of pressure drop in total pressure signal due to the impact of air bubbles on the sensor head. The former is often larger than the later, leading to slightly underestimated turbulence intensity using Eq. (6). The present estimate was in the same order of magnitude as the data of Cummings and Chanson (1997b) and Brattberg and Chanson (1998) using different measuring techniques in less aerated flow regions.

Fig. 4 presents the jet thickness d_{ADM} measured with acoustic displacement meters along the jet centreline, with comparison to the equivalent clear-water jet thickness d_e, the analytical solution of the continuity and Bernoulli principles d_B, the characteristic locations Y_{10}, Y_{50} and Y_{90} where the void fraction is 10%, 50% and 90% respectively, and Y_{Fmax} where the bubble count rate is maximum. The average ADM data were systematically larger than the equivalent clear water jet thickness d_e and the theoretical thickness d_B, which implied thicker jet on the centreline thus potentially three-dimensional structures in the jet. The standard deviations of ADM data were generally large, corresponding to the occurrence of both free-surface aeration and free-surface waves at the jet free-surface. With increasing discharge, the jet instabilities increased and jet thickness on the centreline became larger in the streamwise direction, as shown in Fig. 4B.

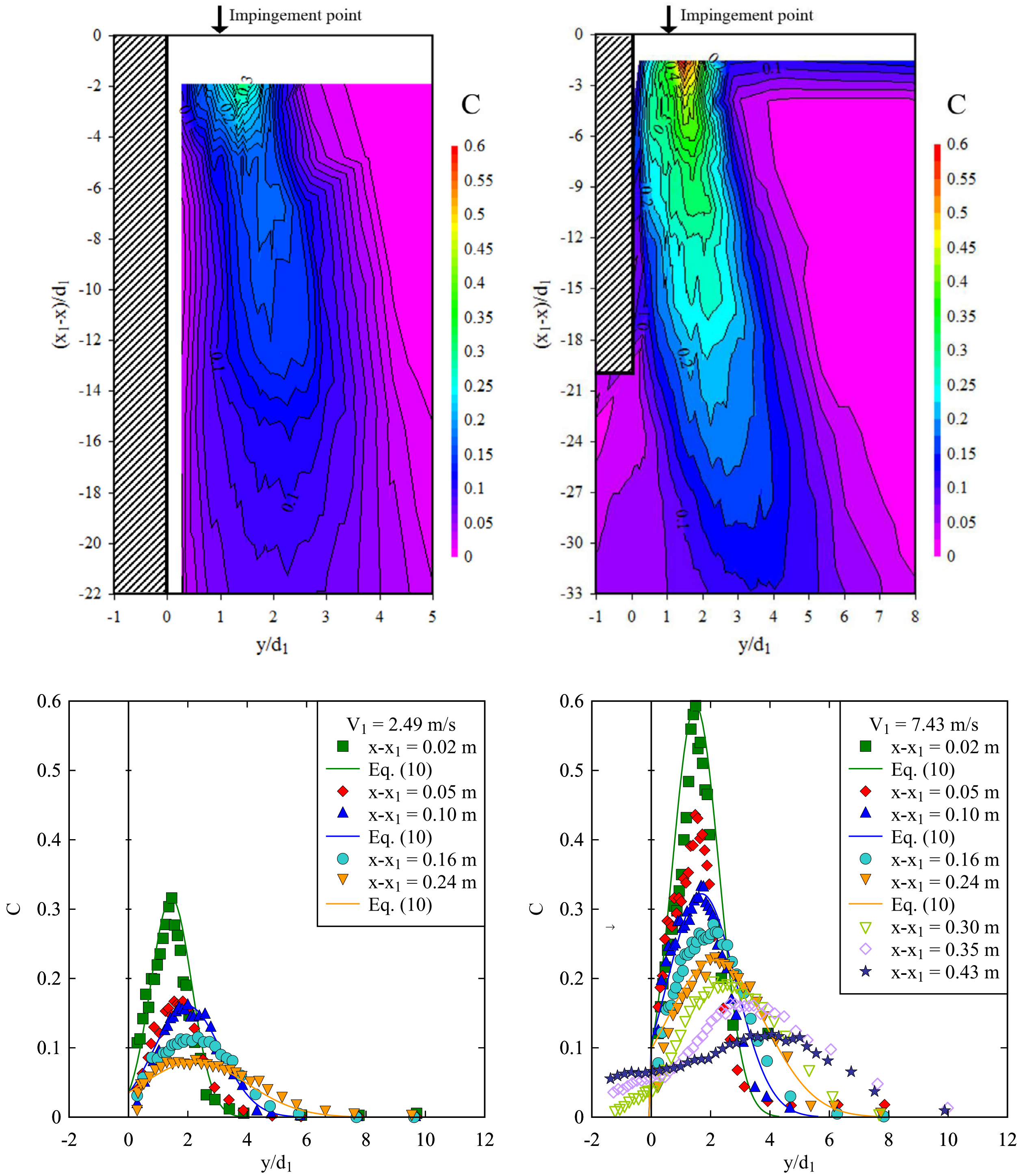

Fig. 5. Dimensionless distributions of time-averaged void fraction – Contour plots: (A, top-left) $V_1 = 2.5$ m/s; (B, top-right) $V_1 = 7.4$ m/s; and cross-sectional profiles with comparison to Eq. (10) at $x-x_1 = 0.02$ m, 0.10 m and 0.24 m: (C, bottom-left) $V_1 = 2.5$ m/s; (D, bottom-right) $V_1 = 7.4$ m/s.

4. Air entrainment and turbulence in plunging pool

4.1. Void fraction, bubble count rate and bubble chord length

A large amount of entrained air was observed below the impingement point for jet impact velocities V_1 larger than the critical onset velocity (Fig. 2B). In the present study, the onset velocity was observed between 0.9 and 1.1 m/s, corresponding to a Weber number from 100 to 120. Air-water flow properties were measured in the large plunge pool's bubbly flow region at several longitudinal locations. Fig. 5 shows typical time-averaged void fraction contour maps (Figs. 5A and 5B) and profiles at different cross-sections (Figs. 5C and 5D) for two impact velocities $V_1 = 2.5$ m/s and 7.4 m/s. In Fig. 5, x_1 is the free-falling jet length and d_1 is the jet thickness at impact. The contour maps highlight the aerated flow regions with the point-source of air entrainment at the impingement point. At each cross-section, the experimental data followed a quasi-Gaussian distribution with a marked maximum value C_{max}. The void fraction profiles flattened as the depth increased, indicating an advective diffusion process. Substantially different void

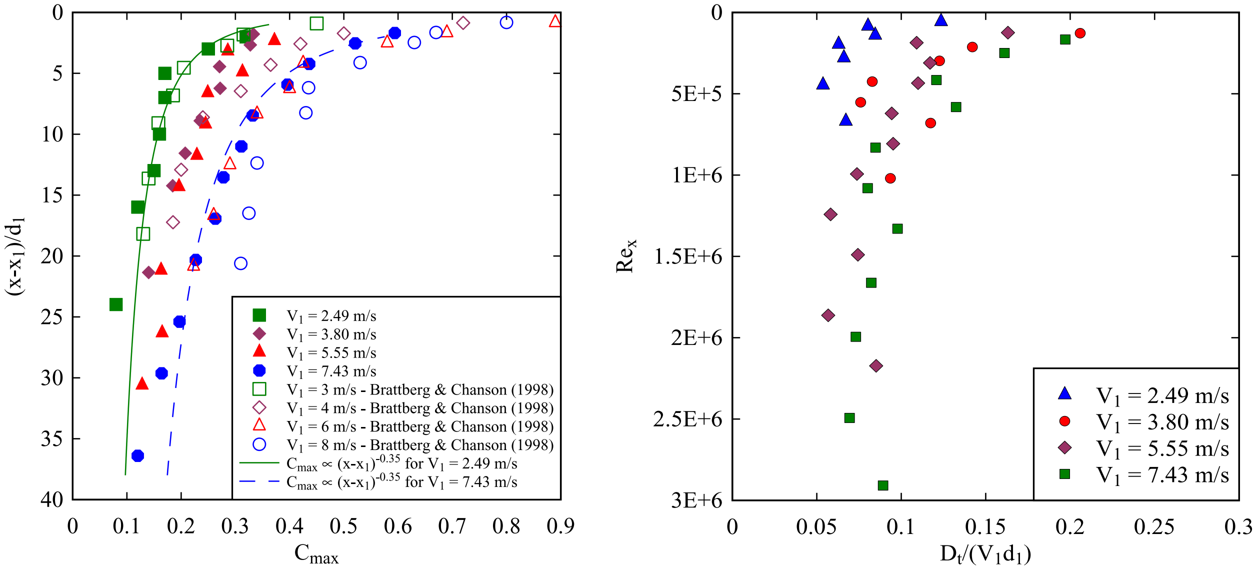

Fig. 6. Longitudinal evolution of maximum void fraction and dimensionless turbulent diffusivity of air bubbles in planar plunging jet: (A, left) Streamwise decay of maximum void fraction; (B, right) Dimensionless turbulent diffusivity as a function of local Reynolds number Re$_x$.

fraction distributions were shown between the two impact velocities. The maximum void fraction at a given cross-section was larger for a higher impact velocity, albeit the void fraction distribution was self-similar. Note that Figs. 5B and D show also an air diffusion process below the jet support, that is, at x-x$_1$ = 0.30 m, 0.35 m and 0.43 m.

For a two-dimensional plunging jet, the air bubble advective diffusion process may be modelled by solving the advective diffusion equation for air bubbles:

$$\frac{V_1}{D_t}\frac{\partial C}{\partial x}=\frac{\partial^2 C}{\partial y^2} \tag{9}$$

where D$_t$ is the cross-sectional average bubble diffusivity (Chanson 1997; Cummings and Chanson 1997a). The analytical solution of Eq. (9), with a boundary condition C = Q$_{air}$/Q$_w$ at (x = x$_1$, y = d$_1$), may be applied to a supported plunging jet using the method of image, yielding:

$$C=\frac{Q_{air}}{Q_w}\frac{\frac{Y_{C_{max}}}{d_1}}{\sqrt{4\pi D^{\#}\frac{x-x_1}{d_1}}}\left(\exp\left(-\frac{1}{4D^{\#}}\frac{\left(\frac{y-Y_{C_{max}}}{d_1}\right)^2}{\frac{x-x_1}{d_1}}\right)\right.$$
$$\left.+\exp\left(-\frac{1}{4D^{\#}}\frac{\left(\frac{y+Y_{C_{max}}}{d_1}\right)^2}{\frac{x-x_1}{d_1}}\right)\right) \tag{10}$$

where Q$_{air}$ is the air flux as a function of the longitudinal distance below the impingement point, Q$_w$ is the water discharge, Y$_{Cmax}$ is the location of maximum void fraction and D$^{\#}$ is a dimensionless diffusivity: D$^{\#}$ = D$_t$/(V$_1$d$_1$). The present experimental data compared well to Eq. (10), as seen in Figs. 5C and D. Note that Eq. (10) yields a relationship between the maximum void fraction C$_{max}$, the dimensionless diffusivity and the relative air entrainment flux:

$$C_{max}=\frac{Q_{air}}{Q_w}\frac{\frac{Y_{C_{max}}}{d_1}}{\sqrt{4\pi D^{\#}\frac{x-x_1}{d_1}}} \tag{11}$$

The maximum time-averaged void fraction data are presented in Fig. 6A as functions of the longitudinal distance below the impingement point. They are compared to the observations of Brattberg and Chanson (1998). Overall the maximum void fraction C$_{max}$ decreased with increasing depth, for all jet impact velocities. The data were best fitted by a power law decay model: $C_{max} \propto (x\text{-}x_1)^{\alpha}$, with an average standard error of 0.0214 and average correlation coefficient of 0.973. The best data fit (i.e. $\alpha = -0.35$) is compared with experimental results in Fig. 6A. For comparison, the previous studies of Chanson (1995) and Brattberg and Chanson (1998) reported $\alpha = -0.44$ and −0. 59, respectively.

Estimate of turbulent diffusivity was based on the best data fit. The results are presented in Fig. 6B as functions of the local Reynolds number defined as Re$_x$ = ρ_wV$_1$(x-x$_1$)/μ$_w$. The present data showed a longitudinal decreasing trend with relatively large turbulent diffusivity immediately below the impingement point. This was inconsistent with the previous findings on comparable air-water turbulent shear flows, e.g. Brattberg and Chanson (1998) on planar plunging jets assuming constant D$_t$ for x-x$_1$ < 0.1 m, and Chanson (2010) and Wang and Chanson (2016) on hydraulic jumps showing a longitudinal increase in diffusivity. In the present study, the high diffusivity coefficient in the downstream vicinity of impingement point was linked to the high jet surface disturbance that resulted in a thickened air-water mixing layer below the impingement point. It has been proved that a reduced inflow disturbance yielded smaller diffusivity close to the impingement point, while the diffusion layer in deep water was not affected, thus the longitudinal variation trend of diffusivity would change. Fig. 6B shows that the turbulent diffusivity approached a constant value between 0.06 < D$_t$/(V$_1$d$_1$) < 0.1 for Reynolds numbers Re$_x$ > 10^6. For comparison, the dimensionless diffusivity ranged from 8 × 10^{-3} to 0.1 in hydraulic jumps (Chanson 2010; Wang and Chanson 2016), from 0.1 to 0.5 in smooth chute flows (Chanson 1997) and from 5 × 10^{-3} to 3 × 10^{-2} on stepped spillways (Zhang and Chanson 2016), albeit some difference might be accounted for different definitions.

For a given void fraction, the bubble count rate F characterises the bubble density and is proportional to the air-water specific interface area. The bubble count rate contours and typical cross-sectional profiles are presented in Fig. 7 in dimensionless form: St = Fd$_1$/V$_1$. The largest number of bubbles was observed in the shear flow region, and a global maximum bubble count rate can be seen at some distance below the impingement point (Figs. 7A & B). At a given cross-section, the bubble count rate profile showed a local maximum F$_{max}$ at a characteristic location Y$_{Fmax}$ (Figs. 7C & D). Fig. 8 illustrates the longitudinal variations of F$_{max}$ and a com-

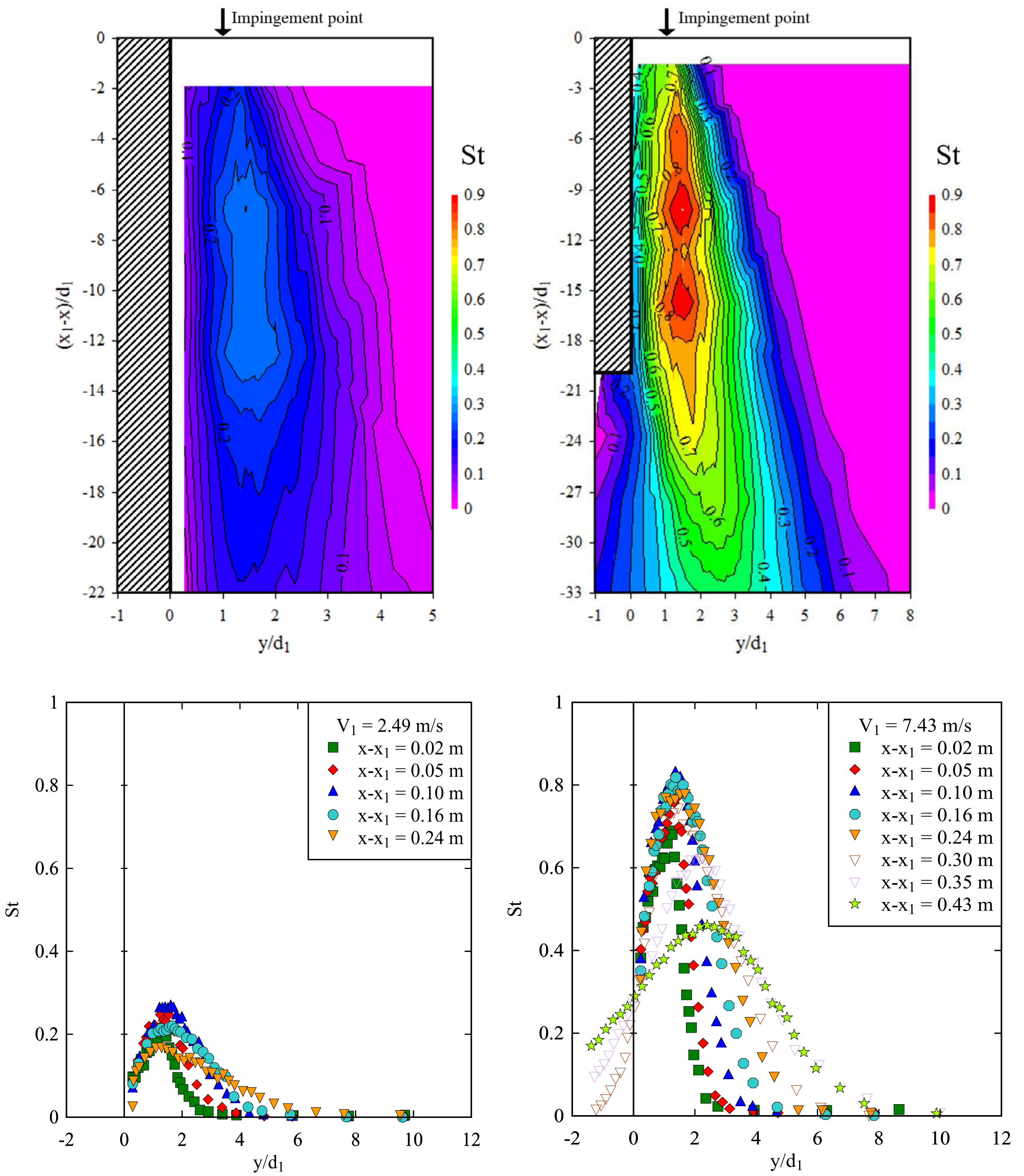

Fig. 7. Dimensionless distributions of bubble count rate – Contour plots: (A, top-left) $V_1 = 2.5$ m/s; (B, top-right) $V_1 = 7.4$ m/s; and cross-sectional profiles: (C, bottom-left) $V_1 = 2.5$ m/s; (D, bottom-right) $V_1 = 7.4$ m/s.

parison with the data of Brattberg and Chanson (1998). Note that a finer phase-detection probe sensor was used in the earlier study, with an inner electrode diameter of Ø = 25 µm, which was able to detect smaller bubbles than the one used in the present work. For all flow conditions, the local maximum bubble count rate increased with increasing jet impact velocity. For a given jet velocity, the longitudinal distributions of maximum bubble count rate exhibited some parabolic shape with increasing depth. This trend suggested that entrained air bubbles were broken up into smaller bubbles immediately downstream of the impingement point, and the characteristic bubble count rate F_{max} reached a longitudinal maximum value for $7 < (x\text{-}x_1)/d_1 < 11$ (Fig. 8). For the present data, the longitudinal maximum was found to increase monotonically with the inflow velocity

$$\frac{(F_{max})_{max} d_1}{V_1} = \frac{1.016}{10^3}\left(\rho_w \frac{(V_1 - V_e) d_1}{\mu_w}\right)^{0.8016} \quad \text{for } 0.9 \text{ m/s} < V_1 < 7.4 \text{ m/s} \tag{12}$$

where V_e is the onset velocity of air bubble entrainment.

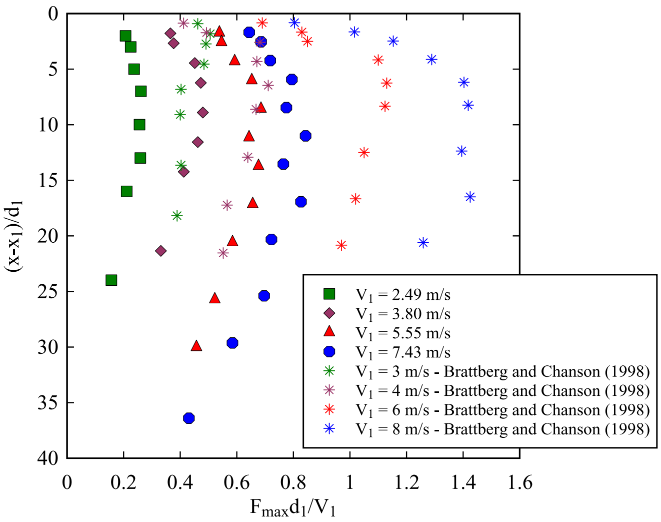

Fig. 8. Longitudinal distributions of maximum bubble count rate below the impingement point – Comparison with data of Brattberg and Chanson (1998) for $x_1 = 0.1$ m.

A comparison between the characteristic positions of maximum void fraction and maximum bubble count rate in a cross-section showed consistently $Y_{Fmax} < Y_{Cmax}$, suggesting that air diffusion layer and developing shear layer did not overlap. The longitudinal variations of the experimental data are respectively correlated by linear relationships:

$$\frac{Y_{C_{max}}}{d_1} = 1.0 + 0.0914\frac{x - x_1}{d_1} \quad \text{for } 0 < \frac{x - x_1}{d_1} < 38 \tag{13}$$

$$\frac{Y_{F_{max}}}{d_1} = 1.0 + 0.0479\frac{x - x_1}{d_1} \quad \text{for } 0 < \frac{x - x_1}{d_1} < 38 \tag{14}$$

with correlation coefficients of 0.874 and 0.789, and standard errors of 0.351 and 0.234, respectively.

The probability distributions of bubble chord length were investigated at these two characteristic locations and further two locations: i.e. one close to the jet support and one at the position of maximum interfacial velocity gradient $(\partial V/\partial y)_{max}$ in the shear layer. Typical results are presented in Figs. 9A and B for two impact velocities at the same longitudinal cross-section. In each graph, the histogram columns represent the probability of a bubble chord length in 0.5 mm intervals from 0 to 10 mm. Generally the data showed similar trends for all impact velocities: $V_1 = 2.5$ m/s to 7.4 m/s. The data exhibited a broad range of bubble chord length at each cross-section from less than 0.5 mm to more than 20 mm. The distributions were skewed with a preponderance of small bubble sizes relative to the mean. A dominant mode in terms of bubble chord length was observed between 0.5 mm and 1.5 mm. The proportion of large bubbles increased with increasing jet impact velocity at a longitudinal cross-section. The bubble chord length data showed the gradual disappearance of largest bubble chord lengths with increasing longitudinal distance below the impingement point. This observation reflected a combination of detrainment of very large bubbles as well as the breakup behaviour of large bubbles in the shear layer. At each cross-section, the average bubble chord increased with increasing distance from the jet support for a given impact velocity, suggesting a larger proportion of small bubbles towards the jet support.

4.2. Bubble clustering

In the bubbly flow of the plunge pool, concentrations of air bubbles separated by short time intervals compared to other bubbly structures were detected, differing substantially from uniformly distributed or randomly distributed bubble populations. The presence of bubbles groups (i.e. bubble clusters) implied that the flow was not fully dispersed, and the advection of bubbles was not a random process. The analysis of particle clustering is relevant in many industrial applications to infer whether the formation frequency responds to particular hydrodynamics frequencies. The level of clustering may further give a quantitative measure of bubble-turbulence interactions and associated turbulent dissipation (Gualtieri and Chanson 2010). Herein a clustering analysis was conducted based upon the signal of the leading phase-detection probe sensor. A near-wake clustering criterion was adopted following previous studies (e.g. Chanson et al., 2006, Wang et al., 2015). With a near-wake criterion, a bubble cluster is defined when the water chord time between two consecutive bubbles is smaller than the air chord time of the leading bubble, suggesting that the trailing bubble was in the near wake of the lead bubble.

Three basic clustering properties were investigated: namely the cluster count rate F_{clu} defined as the number of clusters per second, the average cluster size N_{clu} defined as the average number of bubbles per cluster, and the cluster proportion P_{clu} defined as the percentage of bubbles in clusters. Typical experimental data are presented in Fig. 10. At a given cross-section, the shape of cluster count rate profile was similar to that of bubble count rate profiles, showing maximum values at close positions with magnitude $F_{clu} < F$. The relationship between maximum cluster count rate $(F_{clu})_{max}$ and maximum bubble count rate followed closely a power law:

$$\frac{(F_{clu})_{max} d_1}{V_1} = 0.232\left(\frac{F_{max} d_1}{V_1}\right)^{1.2} \tag{15}$$

The average number of bubbles per cluster ranged from 2 to 4, although most observations were between 2.2 and 2.7. It tended to increase with increasing jet impact velocity at a given cross-section, and for the same jet impact velocity, decrease with increasing depth. The probability distributions of number of bubbles per cluster showed a predominant probability for two bubbles per clusters, typically over 55%, although clusters with more than eight bubbles were consistently detected. This proportion of two-bubble clusters increased with increasing depth, corresponding physically to a longitudinal dissipation of large eddy structures hence a reduction of average cluster size.

Based on their respective definitions, the average cluster size N_{clu} and the proportion of bubbles in clusters P_{clu} must satisfy:

$$P_{clu} = \frac{F_{clu}}{F} N_{clu} \tag{16}$$

Within a short distance below the impingement point, the detection of bubble clusters was affected by the large-scale jet instabilities such as oscillations of impingement position, fluctuations of receiving bath free-surface, and spanwise movements of jet disturbance structures. As a result, large values of average cluster size and cluster proportion were obtained next to the jet support and at the far end of the impingement point. For larger longitudinal distances towards deep water, the bubble clustering behaviour was only affected by the turbulent structures in the shear layer, and the distributions of average cluster size and cluster proportion followed similar trends comparable to that of the unimodal void fraction profiles. The large cluster size and large proportion of bubbles in clusters reflected a combination of high aeration level and intense, anisotropic turbulent motions in the shear flow. The relationship between P_{clu} and N_{clu} was best correlated by:

$$P_{clu} = 0.762\left(1 - e^{-2.025(N_{clu}-2)}\right) \quad \text{for } 2 \le N_{clu} \le 4 \tag{17}$$

with correlation coefficient of 0.959 and standard error of 0.042. The maximum average cluster size $(N_{clu})_{max}$ and maximum cluster proportion $(P_{clu})_{max}$ at a given cross-section decreased with

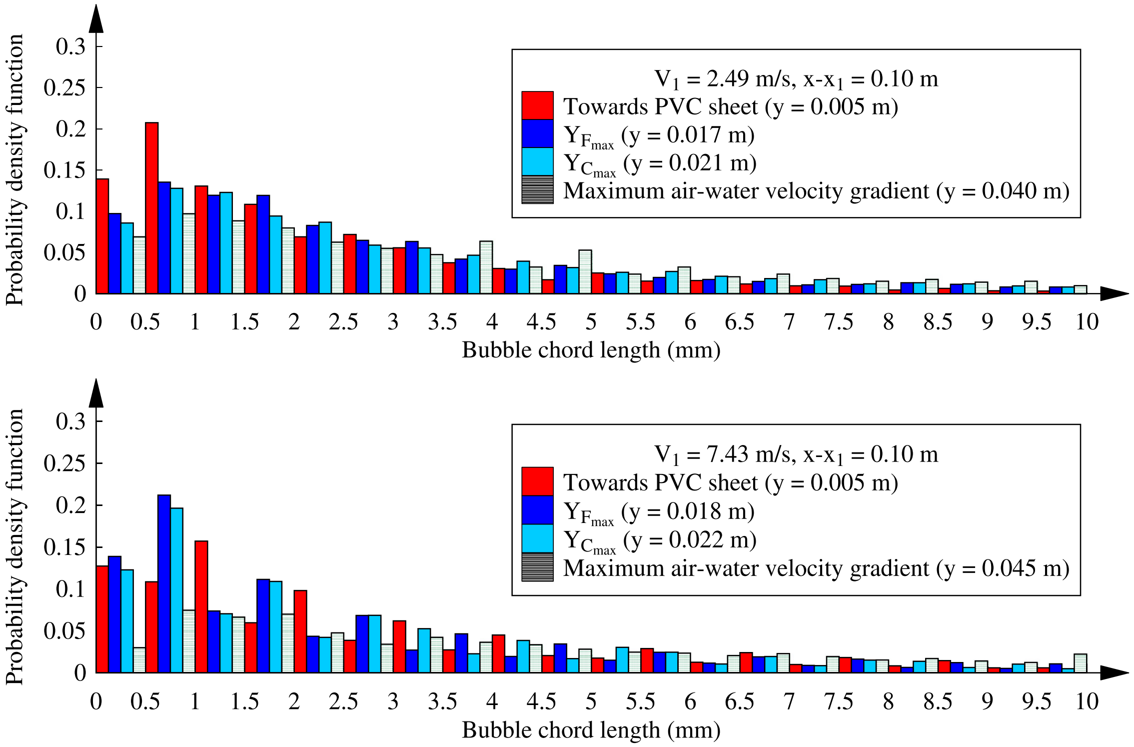

Fig. 9. Probability density functions of bubble chord length in plunging jet flows: (A, top) $V_1 = 2.5$ m/s, x-x$_1 = 0.1$ m; (B, bottom) $V_1 = 7.4$ m/s, x-x$_1 = 0.1$ m.

increasing depth. For smaller jet impact velocities, $(N_{clu})_{max}$ and $(P_{clu})_{max}$ decayed more rapidly over a shorter distance. The former decay rate followed an exponential trend, while the later decay rate followed a linear trend.

4.3. Longitudinal interfacial velocity

Downstream of the impingement point, the air-water flow is basically a free shear layer (Cummings and Chanson 1997b). Momentum is transferred from the high-velocity jet core to entrain the surrounding fluid. Based upon a Prandtl mixing length model, Goertler solved analytically the equation of motion in a free shear layer (Rajaratnam 1976):

$$\frac{V}{V_{max}} = \frac{1}{2}\left(1 - \text{erf}\left(\frac{K(y - y_{0.5})}{x - x_1}\right)\right) \tag{18}$$

where V_{max} is the free-stream velocity, $y_{0.5}$ is the characteristic location where $V = V_{max}/2$, and K derives from the assumption of a constant eddy viscosity $\nu_T = (x\text{-}x_1)V_1/(4K^2)$ across the shear layer. The value of K is inversely proportional to the expansion rate of the momentum shear layer. For monophase shear layers, K is between 9 and 13.5, with a generally accepted value of 11 (Schlichting 1979). The air bubble diffusion of the air-water flows may affect the properties of the shear layer (Brattberg and Chanson 1998).

The contour maps of longitudinal air-water interfacial velocity distributions are presented in Figs. 11A and B, and the data profiles are compared to Eq. (18) at several cross-sections in Figs. 11C and D. Despite some data scatter, large velocity gradient was shown between the jet core and ambient water. The time-averaged interfacial velocity profiles followed closely the theoretical profile. The maximum velocity V_{max} decreased with increasing vertical distance below the impingement point. The present results compared favourably in Fig. 12A with monophase jet literature (Rajaratnam 1976; Chanson 2014). The characteristic location $y_{0.5}$ was found to follow a longitudinal increasing trend (correlation coefficient: 0.886, standard error: 0.446):

$$\frac{y_{0.5}}{d_1} = 2.62 + 0.0865\frac{x - x_1}{d_1} \quad \text{for } 0 < \frac{x - x_1}{d_1} < 38 \tag{19}$$

Below the jet support's end (i.e. x-x$_1 > 0.25$ m), the velocity distribution was affected by the wake of the jet support end, as seen in Figs. 11B and D for the last three cross-sections.

The expansion rate of the developing shear layer is proportional to 1/K. Values of the coefficient K are presented in Fig. 12B and compared to previous studies. The results suggested that K increased with increasing depth, independently of the impact velocity:

$$K = 1.34 + 0.284\frac{x - x_1}{d_1} \quad \text{for } 0 < \frac{x - x_1}{d_1} < 35 \tag{20}$$

The values of K further showed a nonlinear relationship with the maximum void fraction C_{max}, dependent of jet impact velocity V_1:

$$K = 11 - 15.18 C_{max}^{\,0.3\exp(0.152V_1)} \quad \text{for } V_1 < 7.8\,\text{m/s}, C_{max} < 0.6 \tag{21}$$

The correlation coefficients of Eqs. (20) and (21) are 0.959 and 0.915 respectively, with corresponding standard errors of 0.804 and 0.799.

4.4. Auto-correlation time scale and turbulence intensity

The auto-correlation time scale T_{xx} characterised a "lifetime" of the advective bubbly flow structures. Since the bubble clustering analysis showed clearly the non-randomness of bubble distributions and large-scale flow instabilities were visible during experiments, the correlation analysis was expected to yield results larger than those associated with purely random turbulent processes at microscale. Fig. 13 shows typical auto-correlation time scale and interfacial turbulence intensity data within the jet core

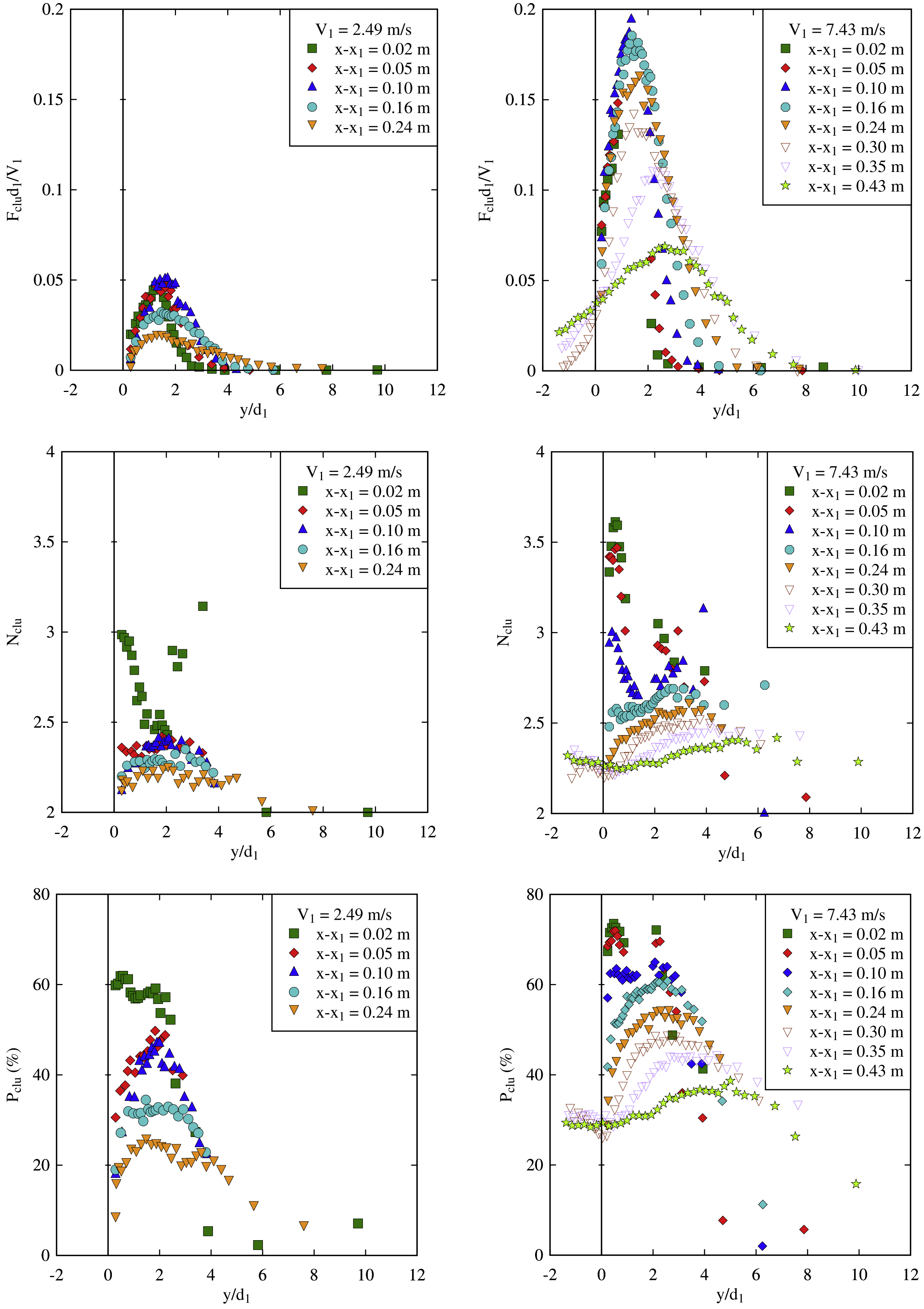

Fig. 10. Dimensionless distributions of bubble clustering properties in plunging jet flows: (A1, top-left) Cluster count rate: $V_1 = 2.5$ m/s; (A2, top-right) Cluster count rate: $V_1 = 7.4$ m/s; (B1, middle-left) Average cluster size: $V_1 = 2.5$ m/s; (B2, middle-right) Average cluster size: $V_1 = 7.4$ m/s; (C1, bottom-left) Cluster proportion: $V_1 = 2.5$ m/s; (C2, bottom-right) Cluster proportion: $V_1 = 7.4$ m/s.

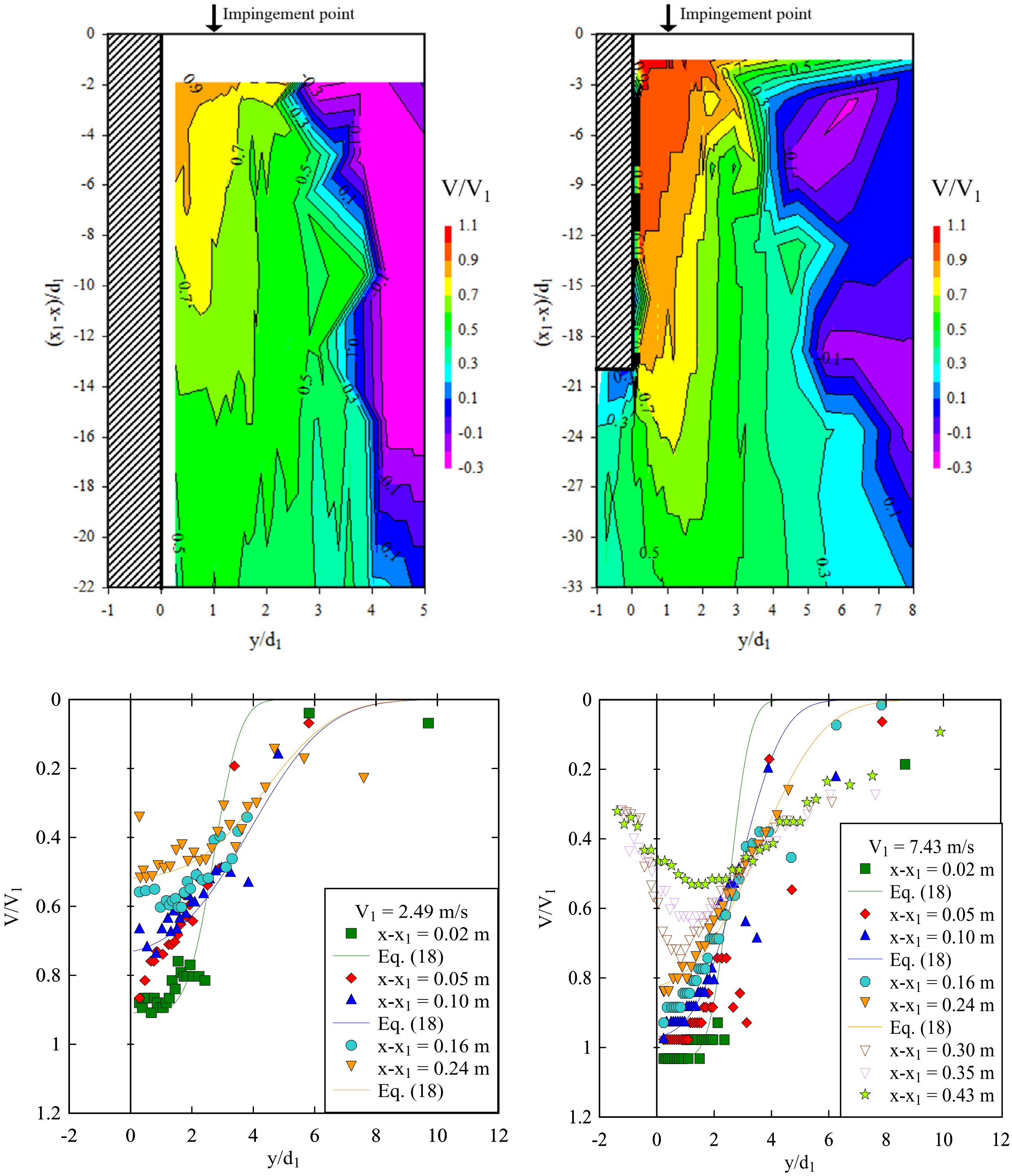

Fig. 11. Distributions of time-averaged air-water interfacial velocity – Contour plots: (A, top-left) $V_1 = 2.5$ m/s; (B, top-right) $V_1 = 7.4$ m/s; and cross-sectional profiles with comparison to Eq. (18) at $x-x_1 = 0.02$ m, 0.10 m and 0.24 m: (C, bottom-left) $V_1 = 2.5$ m/s; (D, bottom-right) $V_1 = 7.4$ m/s.

for the highest investigated impact velocity $V_1 = 7.4$ m/s. At a given cross-section, both data showed a U-shape profile, with a local minimum magnitude between the large values next to the jet support (towards $y = 0$) and in the shear layer (towards $y = y_{0.5}$). On the still-water side of the shear layer, the auto-correlation time scale and interfacial turbulence intensity decayed with increasing distance from the mixing zone (not shown). In the vertical direction, the profile shape tended to be more uniform with increasing depth. The local minimum auto-correlation time scale in the jet core was typically in the order of 10^{-3} s, decreasing streamwise as large turbulent structures dissipated. A similar longitudinal decay was also seen for local minimum interfacial turbulence intensity, although the magnitude was typically as large as 1.2 to 3.2. In the vicinity of the impingement point, a higher jet impact velocity gave larger auto-correlation time scale and turbulence intensity. All auto-correlation time scale data sets converged to a dimensionless minimum value $T_{xx}V_1/d_1 \sim 0.5$ for $(x-x_1)/d_1 > 20$, while the turbulence intensity data to a range of $1 < Tu < 1.2$.

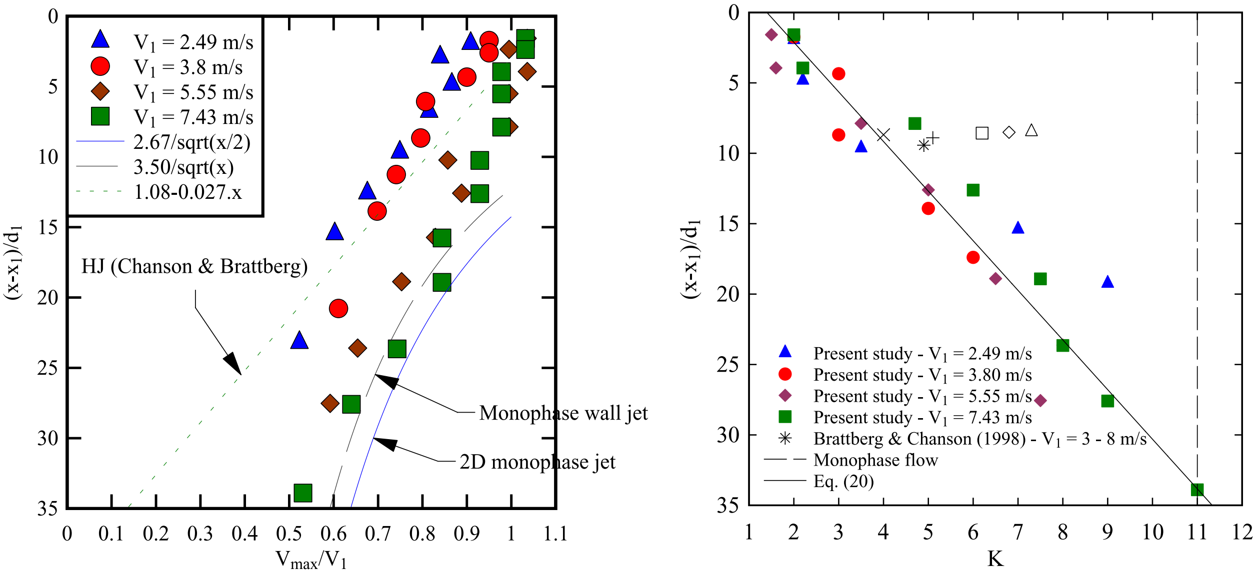

Fig. 12. Longitudinal evolution of maximum interfacial velocity V_{max} and shear layer coefficient K in planar plunging jet: (A, left) Streamwise decay of maximum interfacial velocity, with comparison to hydraulic jump data (Chanson and Brattberg 2000), monophase wall jets (Rajaratnam 1976) and monophase two-dimensional jets (Chanson 2014); (B, right) Streamwise increase in coefficient K, with comparison to air-water flow data of Brattberg and Chanson (1998) and monophase flow observations.

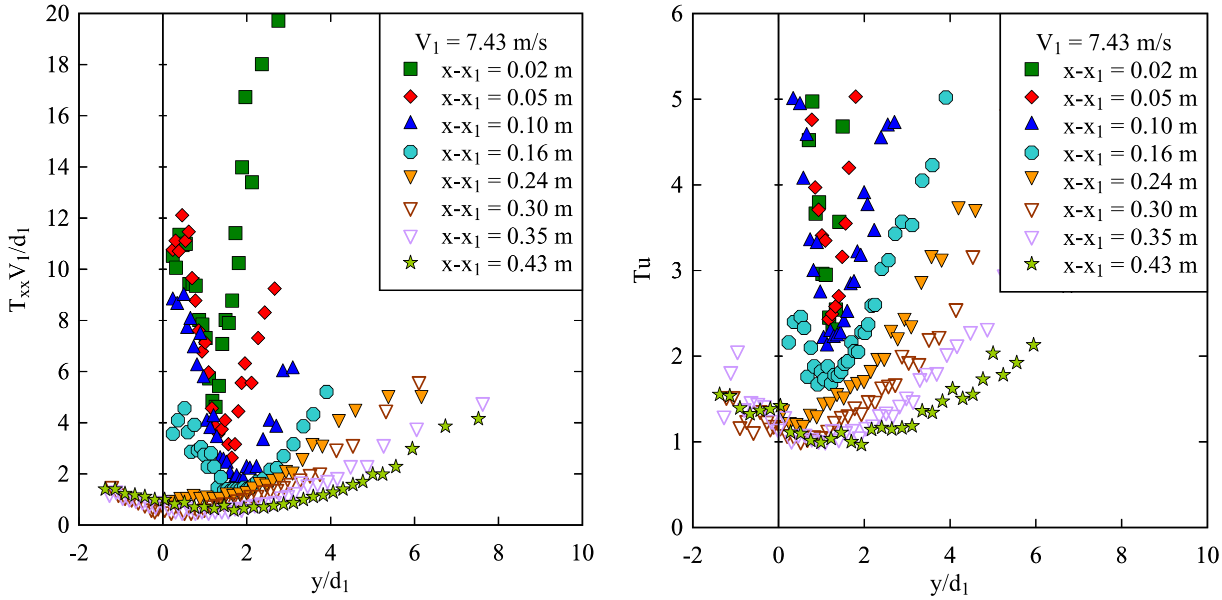

Fig. 13. Auto-correlation time scale and interfacial turbulence intensity distributions underneath the jet core region – $V_1 = 7.4\,m/s$: (A, left) Dimensionless auto-correlation time scale; (B, right) Interfacial turbulence intensity.

Large correlation time scale and turbulence intensity data in the shear layer were known to be linked to the presence of large-scale vortical structures, as also observed in the shear layer of hydraulic jumps (Wang et al., 2014). Herein the large values next to the jet support was unique and believed to relate to the presence of unsteady large jet disturbance structures next to the support boundary due to the three-dimensional flow motions. This was also evidenced by the intense air entity grouping, as suggested in Fig. 10. Practically, the auto-correlation time scale and interfacial turbulence intensity calculated based on correlation analysis provide a measure of the influence of macroscopic jet disturbance, and could be examined when the disturbance effects are of primary concern. A reduced jet instability with modified water supply system upstream of jet nozzle yielded significantly smaller correlation time scale and turbulence intensity next to the jet support. As a result, the local minimum values disappeared, and the profiles shapes were comparable to those in hydraulic jumps underneath the shear layer. The modification of jet condition will be systematically investigated in future work. Lastly, it is noteworthy that the turbulence intensity was overestimated by Eq. (3) because the assumption of random bubble distribution was satisfied and the presence of bubble clusters tended to broaden the correlation functions used to deduce Eq. (3).

5. Air entrainment flux

The air flux was calculated based upon the void fraction and velocity data:

$$q_{air} = \int_0^{+\infty} CVdy \tag{22}$$

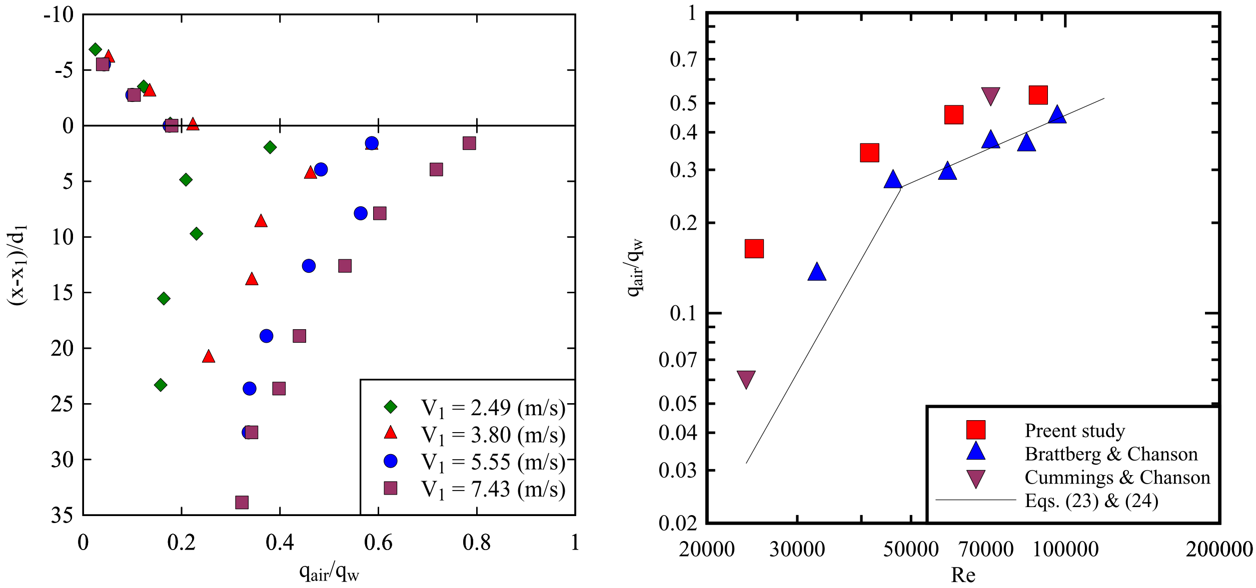

Fig. 14. Dimensionless air flux q_{air}/q_w at vertical planar supported plunging jets: (A, left) Longitudinal evolution of air entrainment rate in free-falling jet and plunging pool; (B, right) Dimensionless air flux in the plunge pool at $(x-x_1)/d_1 = 15$, with comparison to previous data by Cummings and Chanson (1997b) and Brattberg and Chanson (1998).

Both air fluxes in the free-falling jet $(x-x_1 < 0)$ and plunging pool $(x-x_1 > 0)$ were calculated and plotted in Fig. 14A as functions of the longitudinal distance $(x-x_1)$. First the pre-entrainment in the free-jet $(x-x_1 \langle 0)$ was substantial compared to the air flux in the plunge pool, the ratio being between 0.23 and 0.47. Note that the air flux in the jet was integrated from $y = 0$ to $y = Y_{90}$, and a large jet surface roughness contributed to a high pre-entrainment rate under this definition. Below the plunge point, the dimensionless air flux q_{air}/q_w increased with increasing jet impact velocity as previously reported (Ervine and Ahmed 1982; Sene 1988; Brattberg and Chanson 1998). Further q_{air}/q_w decreased with increasing vertical distance below the impingement point for a given jet velocity. This observation differed from the findings of Brattberg and Chanson (1998) who reported no detrainment for $(x-x_1)/d_1 < 17$. Herein the relatively rapid jet deceleration in the plunging pool facilitated the bubble detrainment. A greater entrainment rate was observed close to the impingement point because of the high pre-entrainment level in the jet, although all data sets were close for $(x-x_1)/d_1 \rangle 15$ (Fig. 14B).

The present air flux data are compared to the data of Cummings and Chanson (1997b) and Brattberg and Chanson (1998) in Figure 14B, by comparing the dimensionless air entrainment rate at $(x-x_1)/d_1 = 15$ as a function of the inflow Reynolds number $Re = \rho_w V_1 d_1/\mu_w$. The results showed comparable trends between all data sets, with an increasing air entrainment rate with increasing impact Reynolds number. Further all data showed a significant change in the rate of increase for $V_1 \sim 4$ m/s. Several studies (Van De Sande and Smith 1973; Sene 1988; Brattberg and Chanson 1998) observed the same trend which is believed to be linked to a change in air entrapment mechanism (Bin 1993; Chanson 1997). The correlation proposed by Brattberg and Chanson (1998) were:

$$\frac{q_{air}}{q_w} = \frac{7.7}{10^4}\left(\frac{x_1}{d_1} - 1.04\right)\left(\frac{V_1 - V_e}{\sqrt{gd_1}}\right)^{1.8} \quad \text{for } V_e < V_1 < 4\text{m/s} \tag{23}$$

$$\frac{q_{air}}{q_w} = \frac{2.0}{10^3}\left(\frac{x_1}{d_1} - 1.04\right)\left(\frac{V_1 - V_e}{\sqrt{gd_1}} + 9.3\right) \quad \text{for } 4\text{m/s} < V_1 < 8\text{m/s} \tag{24}$$

Eqs. (23) and (24) are shown in Fig. 14.

6. Conclusion

New experiments were conducted to investigate the air bubble entrainment at supported planar plunging jet. Air-water flow measurements were performed in a relatively large-size facility with constant jet length $x_1 = 0.1$ m and jet impact velocities between $V_1 = 2.5$ m/s and 7.4 m/s, corresponding to partially-developed impingement flow conditions and relatively large jet disturbance.

The free-falling jet flow conditions were documented for nozzle velocities between $V_0 = 2.06$ m/s and 7.30 m/s. A substantial interfacial aeration was observed immediately downstream of the nozzle. The broadening of the free-surface air-water layer was evidenced between the characteristic horizontal positions $y = Y_{10}$ and Y_{90} corresponding to void fractions of 0.1 and 0.9 respectively. The time-averaged void fraction did not always follow the theoretical diffusion solution of free-surface aeration with a constant turbulent diffusivity, suggesting additional aeration sources associated with jet instabilities. Velocity measurements showed that the free jet was partially-developed. Taking into account the air-water flow and assuming zero static pressure in the jet, the turbulence intensity was estimated in an order of 10%.

In the plunge pool, the air-water flow properties were measured with an intrusive phase-detection probe. The advanced instrumentation and data processing techniques supported some earlier findings in literature using similar facilities, while new information was derived with focus on bubble-turbulence interplay. The experiments showed an intense air-water mixing downstream of the impingement point. The development of air diffusion layer and turbulent shear layer was characterised by the streamwise evolution of void fraction, bubble count rate, bubble chord length and interfacial velocity profiles. The void fraction, bubble count rate and interfacial velocity profile shapes were consistent with the literature. The air bubble diffusivity coefficient decreased with longitudinal distance, towards an asymptotic value. The auto-correlation time scale and interfacial turbulence intensity exhibited a U-shape horizontal profile in the vicinity of impingement point, which tended to be more uniform with increasing depth. The correlation analysis gave large correlation time scale and turbulence intensity values next to the jet support and in the outer shear layer because of the effects of large-scale jet fluctuating motions. The bubble clustering properties were derived using the near-wake criterion. The cluster count rate was linked to the bubble count rate. A predominant occurrence for two-bubble clusters was observed, although large-size clusters of eight or more bubbles were consistently detected. The air-entrainment rate was derived from the void fraction and interfacial velocity profile measurements. The results compared favourably with the literature, albeit some difference was observed associated with different inflow conditions. The pre-entrained air flux was substantial herein, and affected the air entrainment process at impingement.

Compared to the previous study of Brattberg and Chanson (1998) using similar jet nozzle facility but different phase-detection sensor diameter, sampling frequency and sampling duration, the results indicated that a larger number of bubbles were detected per unit time with finer sensors, although the present jet conditions were characterised with larger disturbance and pre-aeration.

Acknowledgements

The authors thank Dr Gangfu Zhang (The University of Queensland) for providing programming assistance and Jason Van Der Gevel (The University of Queensland) for laboratorial technical support. They thank Dr Frédéric Murzyn (ESTACA-Laval, France) for his detailed review of the original technical report and his valuable comments. The financial support of the Australian Research Council (ARC DP120100481) and of the University of Queensland is acknowledged.

Appendix A

Table A1
Air–water experimental investigations of planar supported plunging jets.

Reference	x_1 (m)	d_1 (m)	V_1 (m/s)	Tu_1	Re (-)	Main instrument	Sensor size (mm)	Sampling rate (Hz)	Sampling duration (s)	Signal processing outputs
Chanson (1995)	0.09	0.010 to 0.012	2.39 to 9.0	–	2.4×10^4 to 1.1×10^5	Single-tip phase-detection	0.35	Analog integration	180	Void fraction
Cummings & Chanson (1997a,b)	0.0875	0.010 & 0.0117	2.39 & 6.14	~0.01	2.4×10^4 & 7.1×10^4	Dual-tip phase-detection	0.025	40,000	2	Void fraction, Interfacial velocity, Bubble chord sizes
Brattberg & Chanson (1998)	0.05 to 0.15	0.009 to 0.0121	2.0 to 8.0	0.017 to 0.03	1.8×10^4 to 9.7×10^4	Dual-tip phase-detection	0.025	40,000	3	Void fraction, Interfacial velocity, Bubble count rate, Bubble chord sizes
Chanson & Brattberg (1998)	0.09	0.009 to 0.0116	2.0 to 4.0	–	1.8×10^4 to 4.6×10^4	Conical hot-film	0.3	40,000	–	Void fraction, Water phase velocity, Turbulence intensity
Present study	0.10	0.0104 to 0.127	2.49 to 7.43	~0.1	2.6×10^4 to 9.4×10^4	Dual-tip phase-detection	0.25	20,000	90	Void fraction, Interfacial velocity, Bubble count rate, Turbulence intensity, Auto-correlation time scale, Bubble chord sizes, Bubble clustering

Notes: Q: flow rate; d_0: jet thickness at nozzle; V_0: jet velocity at nozzle; x_1: jet length; d_1: jet thickness at impingement point; V_1: impact velocity; Tu_1: jet turbulent intensity at impingement; *Re*: Reynolds number, $Re = \rho_w V_1 d_1 \mu_w{}^{-1}$; (–): information not available.

References

Bertola, N.J., Wang, H., and Chanson, H. (2017). "Air bubble entrainment at vertical plunging jets: a large-scale experimental study." Hydraulic Model Report No. CH104/17, School of Civil Engineering, The University of Queensland, Brisbane, Australia, 256 pp.

Bin, A., 1993. Gas entrainment by plunging liquid jets. Chem. Eng. Sci. 48 (21), 3585–3630.

Bombardelli, F.A., 2012. Computational multi-phase fluid dynamics to address flows past hydraulic structures. In: Matos, J., Pagiliara, S., Meireles, I. (Eds.), Proceedings of 4th IAHR International Symposium on Hydraulic Structures. 9-11 February, Porto, Portugal. Keynote lecture, p. 19.

Bonetto, F., Lahey, R., 1993. An experimental study on air carry under due to a plunging liquid jet. Int. J. Multiphase Flow 19, 281–294 Discussion: 1994, 20(3): 667-770.

Brattberg, T., Chanson, H., 1998. Air entrapment and air bubble dispersion at two-dimensional plunging water jets. Chem. Eng. Sci. 53 (24), 4113–4127.

Chanson, H., 1995. Air entrainment in two-dimensional turbulent shear flows with partially developed inflow conditions. Int. J. Multiphase Flow 21 (6), 1107–1121. doi:10.1016/0301-9322(95)00048-3.

Chanson, H., 1997. Air Bubble Entrainment in Free-Surface Turbulent Shear Flows. Academic Press, London, UK, p. 401.

Chanson, H., 2010. Convective transport of air bubbles in strong hydraulic jumps. Int. J. Multiphase Flow 36 (10), 798–814. doi:10.1016/j.ijmultiphaseflow.2010.05.006.

Chanson, H., 2013. Hydraulics of aerated flows: qui pro quo? J. Hydraulic Res. 51 (3), 223–243. doi:10.1080/00221686.2013.795917.

Chanson, H., 2014. Applied Hydrodynamics: An Introduction. CRC Press, Taylor & Francis Group, Leiden, The Netherlands, p. 448. 21 video movies.

Chanson, H., Aoki, S., Hoque, A., 2006. Bubble entrainment and dispersion in plunging jet flows: freshwater versus seawater. J. Coastal Res. 22 (3), 664–677. doi:10.2112/03-0112.1.

Chirichella, D., Gomez Ledesma, R., Kiger, K., Duncan, J., 2002. Incipient air entrainment in a translating axisymmetric plunging laminar jet. Phys. Fluids 14, 781–790 Discussion: 2002, 14(9): 3367-3368.

Cummings, P.D., Chanson, H., 1997a. Air entrainment in the developing flow region of plunging jets – part 1: theoretical development. *J. Fluids Eng.*, Trans. ASME 119 (3), 597–602.

Cummings, P.D., Chanson, H., 1997b. Air entrainment in the developing flow region of plunging jets – part 2: experimental. *J. Fluids Eng.*, Trans. ASME 119 (3), 603–608.

Cummings, P.D., Chanson, H., 1999. An experimental study of individual air bubble entrainment at a planar plunging jet. *Chemical Engineering Research and Design*, Trans. IChemE, Part A 77 (A2), 159–164.

Ervine, D.A., 1998. Air entrainment in hydraulic structures: a review. In: Proceedings of Institution of Civil Engineers, Water, Maritime & Energy, 130. UK, pp. 142–153.

Ervine, D.A., Ahmed, A.A., 1982. A scaling relationship for a two-dimensional vertical dropshaft. In: Proc. Intl. Conf. on Hydraulic Modelling of Civil Engineering Structures. Coventry, UK. BHRA Fluid Eng., pp. 195–214.

Gualtieri, C., Chanson, H., 2010. Effect of Froude number on bubble clustering in a hydraulic jump. J. Hydraulic Res. 48 (4), 504–508. doi:10.1080/00221686.2010.491688, (ISSN 0022-1686).

Henderson, F.M., 1966. Open Channel Flow. MacMillan Company, USA.

Kiger, K., Duncan, J., 2012. Air-entrainment mechanisms in plunging jets and breaking waves. Annu. Rev. Fluid Mech. 44, 563–596.

Kirchner, W.G., 1974. Gas entrainment by plunging liquid jets. In: Proceedings of 5th Australasian Conference on Hydraulics and Fluid Mechanics. 9-13 Dec, Christchurch , New Zealand.

Kirkpatrick, R.D., Lockett, M.J., 1974. The influence of approach velocity on bubble coalescence. Chem. Eng. Sci. 29, 2363–2373.

Kobus, H., 1984. Scale effects in modelling hydraulic structures. In: Proceedings of International Symposium on Scale Effects in Modelling Hydraulic Structures. Esslingen, Germany. IAHR.

McKeogh, E.J., Ervine, D.A., 1981. Air entrainment rate and diffusion pattern of plunging liquid jets. Chem. Eng. Sci. 36, 1161–1172.

Qu, X.L., Khezzar, L., Danciu, D., Labois, M., Lakehal, M., 2011. Characterization of plunging liquid jets: A combined experimental and numerical investigation. Intl. J. Multiphase Flow 37 (7), 722–731.

Rajaratnam, N., 1976. Turbulent Jet. Elsevier Scientific Publishing Company, Development in water science, 5, New York, USA.

Rao, N.S.L., Kobus, H.E., 1971. Characteristics of Self-Aerated Free-Surface Flows. Water and Waste Water/Current Research and Practice, Vol. 10. Eric Schmidt Verlag, Berlin, Germany.

Richards, J., Lenhof, A., Beris, A., 1994. Dynamic breakup of liquid–liquid jets. Phys. Fluids 6, 2640–2655.

Schlichting, H., 1979. Boundary Layer Theory 800.

Sene, K.J., 1988. Air entrainment by plunging jets. Chem. Eng. Sci. 43 (10), 2615–2623.

Soh, W., Khoo, B., Yuen, W., 2005. The entrainment of air by water jet impinging on a free surface. Exp. Fluids 39 (3), 498–506. doi:10.1007/s00348-005-0965-9.

Van De Donk, J, 1981. Water aeration with Plunging Jets. TH Delft, The Netherlands, p. 168.

Van de Sande, E., Smith, J.M., 1973. Surface entrainment of air by high velocity water jets. Chem. Eng. Sci. 28, 1161–1168.

Van de Sande, E, Smith, J.M., 1976. Jet break-up and air entrainment by low velocity turbulent water jets. Chem. Eng. Sci. 31, 219–224.

Wang, H., Chanson, H., 2016. Self-similarity and scale effects in physical modelling of hydraulic jump roller dynamics, air entrainment and turbulent scales. Environ. Fluid Mech. 16 (6), 1087–1110. doi:10.1007/s10652-016-9466-z.

Wang, H., Felder, S., Chanson, H., 2014. An experimental study of turbulent two-phase flow in hydraulic jumps and application of a triple decomposition technique. Exp. Fluids 55 (7), 18. doi:10.1007/s00348-014-1775-8.

Wang, H., Hu, Z., Chanson, H., 2015. Two-dimensional bubble clustering in hydraulic jumps. Exp. Thermal Fluid Sci. 68, 711–721. doi:10.1016/j.expthermflusci.2015.07.006.

Wang, H., Leng, X., Chanson, H., 2017. Bores and hydraulic jumps. Environmental and geophysical applications. Eng. Comput. Mech. 170 (1600025), 18. doi:10.1680/jencm.16.00025.

Wood, I.R., 1991. Air entrainment in free-surface flows. In: IAHR Hydraulic Structures Design Manual No. 4, Hydraulic Design Considerations. Balkema Publ., Rotterdam, The Netherlands, p. 149.

Zhang, G., Chanson, H., 2016. Interactions between free-surface aeration and total pressure on a stepped chute. Exp. Thermal Fluid Sci. 74, 368–381. doi:10.1016/j.expthermflusci.2015.12.011.

Zhang, G., Chanson, H., Wang, H., 2016. Total pressure fluctuations and two-phase flow turbulence in self-aerated stepped chute flows. Flow Measure. Instrum. 51, 8–20. doi:10.1016/j.flowmeasinst.2016.08.007.

Zhu, Y.G., Oguz, H.N., Properetti, A., 2000. On the mechanism of air entrainment by liquid jets at a free surface. J. Fluid Mech. 404, 151–177.